Airflow and Precipitation Fields within Deep Alpine Valleys Observed by Airborne Doppler Radar*

OLIVIER BOUSQUET
Department of Atmospheric and Oceanic Sciences, McGill University, Montreal, Quebec, Canada

BRADLEY F. SMULL+
NOAA/National Severe Storms Laboratory, Norman, Oklahoma

(Manuscript received 13 August 2002, in final form 24 March 2003)

ABSTRACT

Although airborne Doppler radar is increasingly relied upon to provide detailed descriptions of mesoscale precipitation systems in remote and complex meteorological settings, the utility of these observations has often been limited by the considerable difficulty in their manual processing to remove ground clutter and other sources of contamination, which is a prerequisite to synthesis of reliable airflow and reflectivity fields. This difficulty is further magnified over mountainous terrain, where these sources of contamination take on increased spatial extent and geometric complexity. Removal of such contamination has traditionally required tedious and time-consuming manual editing. As such, routine retrieval of near-surface airflow and precipitation characteristics over steep orography and within hydrologically critical zones, such as deep valleys cutting through mountainous regions (along which population and transportation corridors are frequently concentrated), has been impractical. A new approach is described that largely automates this data-editing procedure for airborne radar platforms, achieving reliable elimination of corrupted data with minimal loss of meteorological signal. Subjective decisions are minimized through a judicious combination of data renavigation, pattern recognition, and reliance upon high-resolution digital terrain information. This technique is applied to data obtained over the Alps by the NCAR Electra and NOAA P-3 aircraft during the recent Mesoscale Alpine Programme field campaign. Three-dimensional airflow and reflectivity fields are shown to illustrate the power and fidelity of this new approach by capitalizing on data collected near, and even beneath, the aircraft track to provide a unique and highly illuminating description of airflow deep within Alpine river valleys and their tributaries during two contrasting orographic precipitation events. The validity of these results is explored through quantitative comparison of this output with independent kinematic measures obtained from ground-based Doppler radar. The utility of airborne radar to provide comprehensive and near-simultaneous views reaching into multiple valleys hidden from the view of ground-based radars is highlighted for a notable case of ''down valley'' flow, more comprehensively illustrating the nature and extent of low-level upstream blocking during a widespread orographic precipitation event.

1. Introduction

Because of their uniquely elevated location, unmatched mobility, and vertical sampling strategy, airborne Doppler radars are increasingly coming into use to investigate precipitation processes over poorly accessible areas, such as steep and convoluted mountain slopes. A number of important field campaigns involving airborne radar platforms have been mounted in the last several years to identify processes leading to devastating floods and other forms of severe weather both over and adjacent to regions of mountainous terrain. These efforts include the Coastal Observation and Simulations with Topography experiment (COAST, Bond et al. 1997), with phases I and II being conducted over the Pacific Northwest in 1993 and 1995, respectively; the California Landfalling Jets Experiment/Pacific Landfalling Jets Experiment (CALJET/PACJET; Ralph et al. 1999), focusing on the mountainous California coastline and adjacent Pacific waters during 1998–2001; the Mesoscale Alpine Programme (MAP; Bougeault et al. 2001), conducted over the European Alps in 1999; the Intermountain Precipitation Experiment (IPEX; Schultz et al. 2002), focusing on the Wasatch range and adjacent Great Salt Lake basin of Utah in February of 2001; and, most recent, the second phase of the Improvement of Microphysical Parameterization through Observational Verification Experiment (IMPROVE-II; Stoelinga et al. 2003), conducted over the central Oregon Cascades during late 2001. Because of difficulties in siting ground-based instruments and because of pervasive beam block-

* National Oceanic and Atmospheric Administration Contribution Number 1008.

+ Current affiliation: Department of Atmospheric Sciences, University of Washington, Seattle, Washington.

Corresponding author address: Dr. Olivier Bousquet, Department of Atmospheric and Oceanic Sciences, McGill University, 805 Sherbrooke W., Montreal, QC H3A-2K6, Canada.
E-mail: bousquet@zephyr.meteo.mcgill.ca

© 2003 American Meteorological Society

Unauthenticated | Downloaded 03/11/24 09:28 PM UTC

ing in regions of rugged terrain, many scientific opportunities presented by these programs hinge on the proper analysis of airborne Doppler radar datasets, which offer a unique means to collect detailed information on terrain-forced phenomena and to relate them to the larger-scale mesosynoptic environments in which they develop. On the other hand, the topographic and meteorological complexity characteristic of mountainous regions serve to complicate greatly and thus slow the processing of these datasets, with the unfortunate outcome that a large fraction of available observations may effectively be ignored owing to practical considerations. For instance, with the exception of Colle and Mass (1996) and Colle et al. (1999), who conducted studies of steady and frontally modulated flow around the Olympic mountains during COAST intensive observation periods (IOPs) 4 and 5, respectively, virtually all studies that have emerged from COAST and CALJET have been confined to zones adjacent to or even farther removed from zones of steep terrain. This relative dearth of analyses that capitalize on data collected directly over mountainous terrain is indicative of the difficulties in analyzing airborne radar datasets over mountainous regions.

Prior to MAP, a number of investigators have sought to improve methods for processing radar observations collected by airborne radar platforms operating over mountainous regions. For instance, Georgis et al. (2000) used exploratory data collected over the U.S. Rocky Mountains to develop a method to identify and minimize errors in aircraft navigation and radar beam-pointing angles and, hence, to evaluate more accurately the horizontal and vertical components of wind over complex terrain. Chong and Cosma (2000) further proposed a new formulation of the mass continuity equation, applicable to either flat or complex terrain, to be implemented in the multiple-Doppler synthesis and continuity adjustment technique (MUSCAT; Bousquet and Chong 1998; Chong and Bousquet 2001), whose utilization was formerly restricted to radar observations collected over flat lands and oceans. Application of these techniques to airborne data collected during MAP has already led to several studies aimed at improved understanding of the complex processes involved in the formation of precipitation over mountainous regions. Among those, Pradier et al. (2002; who studied the dynamics and momentum transports within a convective line observed in MAP IOP 5) and Bousquet and Smull (2003; who describe regional-scale aspects of upstream blocking and associated kinematic and reflectivity structures during the MAP IOP 8 heavy-rain event) provide examples of the capabilities possessed by airborne Doppler radars over such broad and poorly accessible regions. Another vivid illustration of their unique utility over steep terrain can be found in Steiner et al. (2003), who investigated the airflow within a deep Alpine valley under heavy rainfall and demonstrated that a pronounced and unexpected (Bougeault et al. 2001) downslope flow could be observed during several MAP IOPs. As evidenced by events such as the Big Thompson Canyon flood in the U.S. Rocky Mountains (Caracena et al. 1979), observations of precipitation rates and airflow within deep mountain drainages can be of profound importance in illuminating the dynamics of events of severe orographic weather events.

The aim of this paper is to illustrate the capacity of airborne radar systems to map low-level wind and reflectivity fields over complex orography by investigating airflow and precipitation structures within multiple deep Alpine valleys and their tributaries and to elaborate on advances in objective processing techniques that make these analyses possible. Data from two contrasting heavy-rain events on the south-facing slopes of the Alps are considered: the more convectively unstable case of MAP IOP 2b (20 September 1999) and an episode of lighter but more widespread and prolonged stratiform precipitation observed during IOP 8 (21 October 1999). This analysis generalizes and extends the findings of Steiner et al. (2003) concerning the existence of subsiding down-valley flow, which was previously shown in detail for only a single valley (that of the Toce River), by providing contemporaneous observations within other diversely oriented Alpine valleys throughout the Lago Maggiore region during MAP IOP 8.

2. Methods

a. Data editing

In contrast with volume scans obtained by ground-based radars, for which only the lowest elevation angles routinely intercept the earth's surface, each and every sweep from helically scanning airborne radars strikes the earth's surface and, thus, contains associated ground-clutter contamination. If not completely removed, this contamination can strongly bias the estimates of Doppler velocity and reflectivity in the critical near-surface layer. This is particularly true over mountainous regions, where tremendous topographical variability tends to greatly enhance and complicate signal returns from nonmeteorological targets. Figure 1 presents a view of a single 360° sweep of raw (Figs. 1a–d) radial velocity and reflectivity data collected over the Alps by the tail Doppler radar aboard the National Oceanic and Atmospheric Administration (NOAA) P-3 aircraft over a 6-s interval, ending at 0913:35 UTC 21 October 1999. Four main difficulties can be identified: (i) an intense and irregular pattern of reflectivity values reaching 65 dB*Z* that defines the signature of the earth's surface (ground clutter), (ii) range-folded echoes (often referred to as ''second trip'' returns) that result from the radial dislocation of legitimate echoes actually located beyond the maximum unambiguous range (R_{max}), (iii) sidelobe returns resulting from the influence of energy transmitted and/or subsequently received from directions

Unauthenticated | Downloaded 03/11/24 09:28 PM UTC

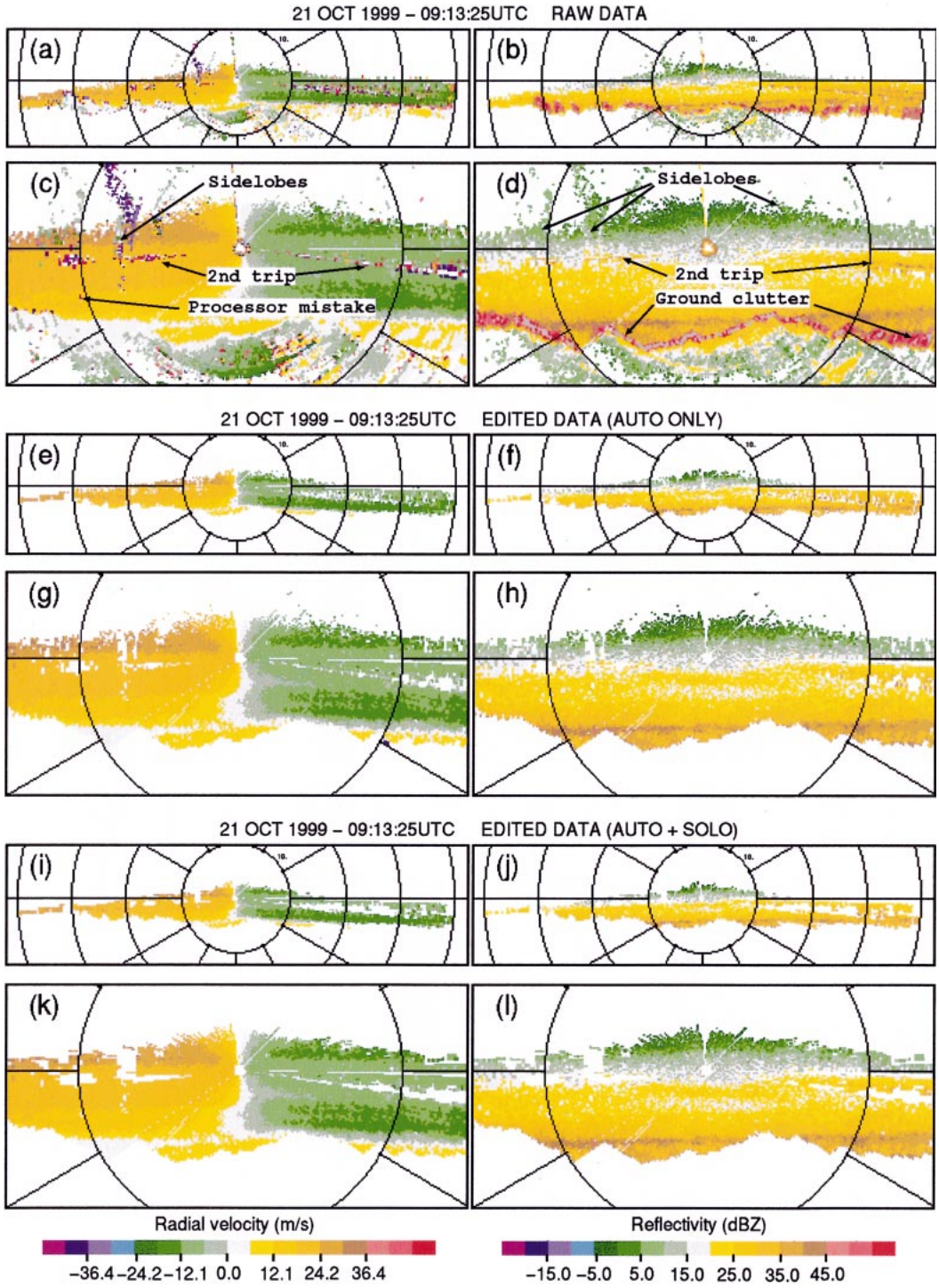

FIG. 1. Quasi-vertical scans by the fore antenna of the NOAA P-3 N42RF tail Doppler collected over the Italian Alps at 0913:35 UTC 21 Oct 1999. Left and right panels present radial velocities (m s^{-1}) and reflectivity (dB*Z*), respectively. Range rings and elevation angles are shown every 10 km and 30°. Lower panels show observations at close range (<15 km) from the radar. (a)–(d) ''Raw'' (unedited) data; (e)–(h) and (i)–(l) results after application of the ''automated'' and ''automated + manual'' editing techniques, respectively.

Unauthenticated | Downloaded 03/11/24 09:28 PM UTC

well off the most intensely focused portion (main axis or ''lobe'') of the radar beam, and (iv) isolated unrealistic values of the velocity measurements over the extended Nyquist interval [known as ''processor mistakes'' (Jorgensen et al. 2000)], which are specific to dual pulse repetition frequency (PRF) schemes recently implemented in airborne systems. As illustrated by Fig. 1, second-trip, sidelobe, and processor mistake phenomena occur in the free atmosphere and are frequently associated with discontinuities of radial velocity in the along-beam direction, whereas ground-clutter contamination is most dependably identified by a strong discontinuity in the reflectivity field. This discontinuity tends to be most pronounced at a high incidence angle, which in the limiting case of uniform (flat) terrain is achieved directly beneath the aircraft and decreases with offtrack distance. The principle of the approach described herein is to profit from these signatures to identify and eliminate these various sources of contamination via a four-step process.

First, radar data must be ''renavigated'' to ensure their accurate location in a three-dimensional framework even in the presence of systematic errors in radar beam positioning that may occur for airborne platforms. In the context of minimizing such errors, the presence of highly variable (and thus uniquely patterned) terrain is actually an advantage. Ground clutter is first objectively identified using a combination of prominent discontinuities in the observed reflectivity pattern for those beams falling within 45° of the nadirmost beam in each sweep and digital terrain data. The observed topology of this clutter pattern (as defined from a series of sweeps along a flight-track segment) is then compared with that expected based upon an independent digital terrain map (DTM) of 30-s lat/lon (~750 m) resolution. Following the method of Georgis et al. (2000), minimization of the differences between these two clutter maps may effectively be used to eliminate systematic errors in measured versus actual aircraft attitude/position variables and aircraft-relative beam pointing angles.

The second step is to process these renavigated radar data objectively so as to remove the ground-clutter contamination. For those beams along which well-defined surface-generated discontinuity of reflectivity is encountered, radial data at and beyond that location are discarded. If this reflectivity-based approach fails or is otherwise not applicable (e.g., for beams falling outside of the aforementioned ±45° window or in the absence of prominent discontinuities), the DTM is again accessed to evaluate the position of each discrete measurement volume (or ''gate'') relative to the ground. Although higher-order radar-processing techniques (such as wind synthesis methods) typically treat radar data as a set of point measurements, for this application it is important to account for the finite volume represented by each datum. As shown in Fig. 2 for a Cartesian framework with x and y axis pointing eastward and northward, respectively, the location of an individual measurement or gate $M_0(X_{M0}, Y_{M0}, Z_{M0})$, which is commonly identified as the geometric center of its associated pulse-resolution volume, may be defined as

$$\begin{aligned} X_{M0} &= \mathrm{Xrad} + \delta\mathrm{Xrad} \\ &\quad + f(r + \delta r, \Theta + \delta\Theta, R + \delta R, H + \delta H, \\ &\qquad T + \delta T, P + \delta P, D + \delta D), \\ Y_{M0} &= \mathrm{Yrad} + \delta\mathrm{Yrad} \\ &\quad + f(r + \delta r, \Theta + \delta\Theta, R + \delta R, H + \delta H, \\ &\qquad T + \delta T, P + \delta P, D + \delta D), \quad \text{and} \\ Z_{M0} &= \mathrm{Zrad} + \delta\mathrm{Zrad} \\ &\quad + f(r + \delta r, \Theta + \delta\Theta, R + \delta R, T + \delta T, \\ &\qquad P + \delta P), \end{aligned} \tag{1}$$

where Xrad, Yrad, and Zrad account for the location of the radar relative to the Cartesian grid origin; r is the distance of gate M_0 from the radar in the along-beam direction, Θ is the measured rotation angle measured in a plane orthogonal to the antenna's axis of rotation; T is the measured tilt angle (which defines the fore vs aft departure of the beam axis from this plane); R, P, D, and H are respectively the measured roll, pitch, drift, and heading angles of the aircraft; and quantities δ refer to associated renavigation corrections (typically only a few tenths of a degree or hundreds of meters) as derived following the established technique of Georgis et al. (2000) [or, equivalently, Testud et al. (1995) in the case of flat terrain].

The principle of the DTM approach is to use estimated positions (X_{M0}, Y_{M0}, Z_{M0}) to ascertain whether the altitude of a given datum M_0 is above or below the ground, that is, whether altitude Z_{M0} is above or below the earth's surface, $Z_{surf}(X_{M0}, Y_{M0})$, as interpolated from the high-resolution terrain database. However, because each radar datum effectively represents the summed properties of distributed targets within a volume whose size is range dependent, a gate whose center lies above the surface may actually contain a substantial amount of ground return. Gate characteristics depend on the actual resolution of the radar and are a function of three factors: the pulse length $c\tau$, the angular resolution defined by the half-power beamwidth Φ, and the radial resolution Δr. The radial resolution defines the distance between two successive gates, the pulse length accounts for the thickness δr of each gate ($\delta r = 2c\tau$), and the angular resolution, which is a function of the horizontal and vertical beamwidths of the radar, defines its lateral extent. If one considers the case of a circular beam (for which the horizontal and vertical beamwidths Φ are identical, as is the case for the Centre des Environments Terreste et Planetaires (CETP) flat-plate antenna available for use on the NOAA P-3), a radar gate consists to a first approximation of a cylinder of radius $r \sin(\Phi/2)$ and thickness δr (the constant radius assumption being

Unauthenticated | Downloaded 03/11/24 09:28 PM UTC

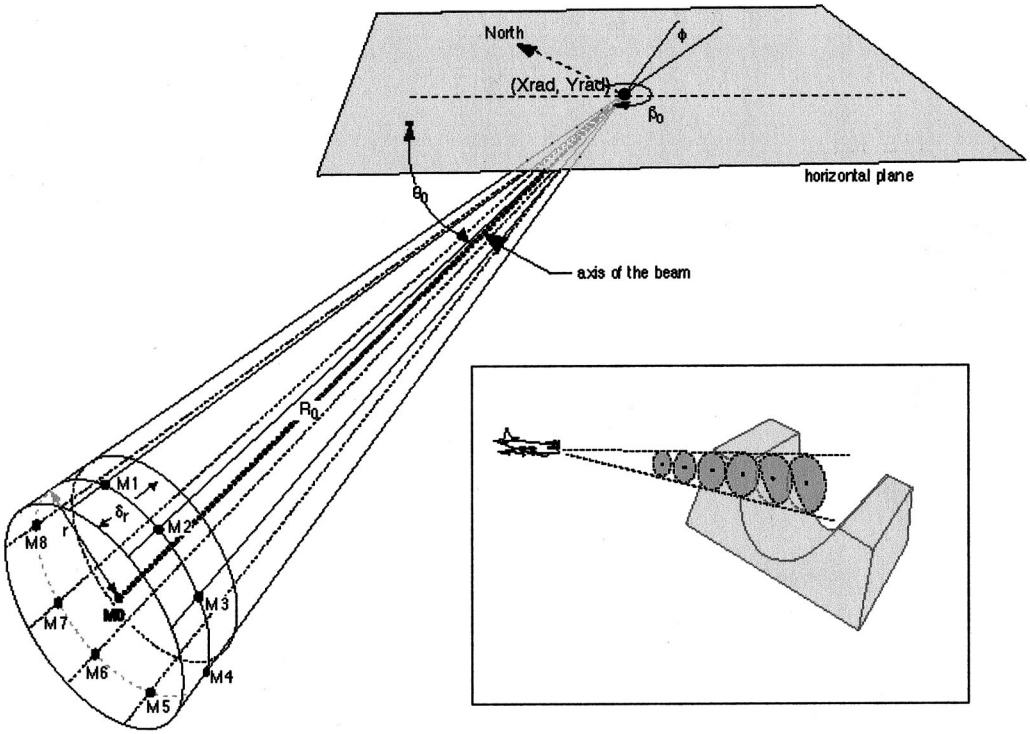

FIG. 2. 3D schematic of a radar beam of angular width ϕ and radial resolution δr, pointing downward in a direction β_0 (with respect to the north) at an elevation θ_0 (with respect to the horizontal), and intercepting a complex surface. Distance R_0 represents the distance between a given gate M_0 and the radar, with respect to the center of a pulse volume of radius r and thickness δr; M1 ($\theta_0 + \phi/2$, $\beta_0 + \phi/2$), M2 ($\theta_0 + \phi/2$, β_0), M3 ($\theta_0 + \phi/2$, $\beta_0 - \phi/2$), M4 (θ_0, $\beta_0 - \phi/2$), M5 ($\theta_0 - \phi/2$, $\beta_0 - \phi/2$), M6 ($\theta_0 - \phi/2$, β_0), M7 ($\theta_0 - \phi/2$, $\beta_0 + \phi/2$), and M8 (θ_0, $\beta_0 + \phi/2$) are regularly spaced points along the circle of radius r centered on M_0 that is perpendicular to the direction of the beam. Inset at the lower-right schematically illustrates a situation in which substantial ground echo return may occur even though the beam's center remains above the surface.

justified by considering typical airborne radar values of 75 m for δr and 2° for Φ). For a gate $M(X_M, Y_M, Z_M)$ located 40 km distant from the radar, this leads to a radius of approximately 700 m. As shown in Fig. 1b, this additional contamination (which we will refer to as the beamwidth effect) is thus particularly important at a long range from the radar, and its effects are dramatically exacerbated when the surface topography is variable.

The principle of the beamwidth correction is to determine if any given point $I(X_{MI}, Y_{MI}, Z_{MI})$ within the measurement volume M intersects the surface (as conceptualized in the inset of Fig. 2) by comparing its altitude Z_{MI} against the one derived from the DTM at the same location (X_{MI}, Y_{MI}). In practice, this additional check is accomplished by examination of eight discrete points (viz., M1–8 in Fig. 2), which are located on a circle of radius r centered on M_0 and oriented perpendicular to the direction of the beam. If any of these peripheral points is found to lie below the surface, the gate is assumed to contain a significant amount of ground return and is, thus, discarded.

In the third stage of processing, radial data are sequentially examined for discontinuities of radial velocity to eliminate artifacts associated with other sources of contamination identified in difficulties ii–iv above. This objective step is based upon a familiar algorithm, usually referred to as a ''running mean'' or ''Bargen and Brown'' (1980) approach, and allows more isolated outliers commonly associated with range-folded echoes and dual-PRF processor mistakes to be largely eliminated. In the case of airborne Doppler data collected in single-PRF mode, which typically have a much smaller Nyquist interval, a variant of this technique is routinely applied to correct velocity aliasing.

Together, these three steps compose the objective part of the editing technique whose performance is shown in Figs. 1e–h for the ''raw'' data previously introduced in Figs. 1a–d. Overall, at both long (Figs. 1e–f) and short (Figs. 1g–h) ranges from the radar, the ground-clutter elimination technique is found to perform very well, with no detectable failures. Farther aloft, the majority of corrupted observations—including those affected by sidelobe contamination and processor mistakes—have been successfully removed, although a few aberrant gates exhibiting remnant effects of second-trip contamination can still be identified in Figs. 1e–f. This limitation rests in the fact that the running-mean ap-

Unauthenticated | Downloaded 03/11/24 09:28 PM UTC

proach is not fully capable of distinguishing between artifacts and real atmospheric variability, for example, as may be encountered in convective or otherwise turbulent environments. Thus, despite the generally reliable performance of the automated approach, a certain amount of interactive (manual) examination is usually required to finalize the editing (Fig. 1i–l). Application of this approach to large volumes of data collected during MAP, IPEX, CALJET/PACJET, and IMPROVE-II orographic precipitation events has shown that the time required for this fourth and final step, as carried out using the National Center for Atmospheric Research (NCAR) Solo software (Oye et al. 1995), is markedly reduced relative to an entirely manual editing approach.

b. Wind synthesis

To retrieve fully three-dimensional wind and reflectivity fields, edited observations are ingested in the MUSCAT analysis proposed by Bousquet and Chong (1998) and recently improved by Chong and Cosma (2000), who proposed a new formulation of the mass continuity equation that can be applied to either flat or complex terrain. MUSCAT is a variational approach aimed at deducing simultaneously the three Cartesian wind components from the global minimization, in a least squares sense, of an ensemble of three cost functions that represent 1) an optimal least squares fit of the observed radial Doppler velocities to the derived wind component, 2) a least squares adjustment with respect to mass continuity, and 3) a second-derivative constraint to minimize small-scale wind variations (i.e., noise). This simultaneous solution eliminates the main drawbacks of iterative techniques commonly employed in multiple-Doppler analysis of airborne and ground-based radar observations (Bousquet and Chong 1998; Chong and Bousquet 2001) and, moreover, allows information to be extracted from above/below the aircraft track (in the case of airborne analysis) or along the baseline that connects each radar pair (for ground-based radar systems). This last point is of particular importance with respect to airborne radar data collected over complex terrain, because some of the most valuable high-resolution observations (including views that extend downward into deep Alpine valleys) are found below the aircraft. A detailed description of MUSCAT, including its numerical development, can be found in the above-cited papers.

Because the three-dimensional wind field reconstructed using MUSCAT represents a least squares fit to the available observations and, hence, does not perfectly satisfy the mass continuity equation, an a posteriori integration is performed that follows the variational method of Georgis et al. (2000) subject to simultaneous minimization of both 1) the horizontal gradient of vertical velocity within the domain of interest and 2) vertical velocity at the upper boundary. The reader may refer to this paper for further details.

3. Valley flow during MAP

a. Datasets

A visually striking and dynamically significant illustration of the capacity of airborne Doppler radar to retrieve detailed airflow and precipitation structure accurately over complex terrain is provided by analysis of observations collected during the September–November 1999 field phase of the Mesoscale Alpine Programme. One of MAP's major objectives is the investigation of orographic precipitation mechanisms and associated severe flooding that frequently occur on the Mediterranean side of the Alps (Bougeault et al. 2001). Results derived using the methods described in section 2 and selected for illustration here are drawn from datasets collected on 20 September 1999 (MAP IOP 2b) by the Electra Doppler radar (ELDORA) Analyse Stereoscopic par Radar Aeroporte sur Electra (ASTRAIA) (Hildebrand et al. 1994), which during MAP was mounted on the NCAR Electra aircraft, and on 21 October 1999 (MAP IOP 8) as observed by an analogous single-transmitter Doppler system carried aboard the NOAA P-3 airplane No. N42RF (e.g., Jorgensen et al. 1983). These data encompass the rugged southern slopes of the Alps and adjacent flat terrain of the Po River basin in northern Italy and include measurements in and around various rifts and deep valleys of the Lago Maggiore region highlighted in Fig. 3. Such views are derived primarily from radial data at close range (viz., immediately adjacent to and below the flight track) and are thus minimally affected by complicating effects of beamwidth. In the case of MAP IOP 8, our airborne results may be further compared with data obtained by a mobile X-band ''Doppler on Wheels'' (DOW) system within the Toce River valley (Steiner et al. 2003) to obtain a quantitative intercomparison of these data-processing and analysis techniques. The notably blocked versus unblocked nature of low-level airflow approaching the Alps during IOPs 8 and 2b, respectively, offers a clear illustration of the variability in airflow regimes and orographic precipitation response that can occur in this region.

b. A case of cellular convective precipitation (MAP IOP 2b)

One of the most significant precipitation events observed during the entire MAP special operations period occurred on 20 September 1999 during MAP IOP 2b (e.g., Medina and Houze 2003) and was associated with the passage of a strong baroclinic disturbance over the Alpine region. The interaction of baroclinically forced south-southwesterly flow with the Alps led to the formation of heavy precipitation over the steep mountain slopes of the climatologically favored Lago Maggiore region. Thermodynamic conditions were relatively unstable on this day, and low-level airflow impinging on the barrier was able to ascend over the steep terrain with

Unauthenticated | Downloaded 03/11/24 09:28 PM UTC

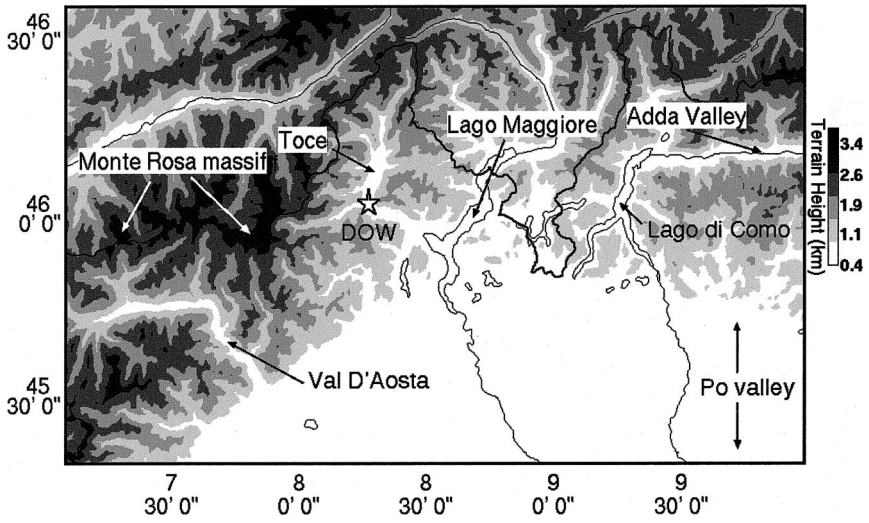

FIG. 3. Topography in the vicinity of the Lago Maggiore region. Heavy and light black lines indicate borders between Switzerland (to the north) and Italy, and lakes and rivers, respectively. Black star shows the location of the DOW radar during MAP IOP 8.

relative ease (Rotunno and Ferretti 2003; Medina and Houze 2003). Synthesized horizontal wind fields and reflectivity patterns at 1.0 and 2.0 km MSL are shown in Fig. 4 for a period during which the Electra made a northeast-bound pass over the Toce River valley (cf. Fig. 3). This deep, L-shaped Alpine valley, which drains southeastward into the Lago Maggiore and ultimately the Po basin, is characterized by sheer walls extending 1000–2000 m above the valley floor and is bordered on the west by the high summits of the Monte Rosa massif (>4000 m MSL).

At the time of Fig. 4, the radar reflectivity pattern was characterized by numerous (though sometimes rather shallow) convective cells confined principally to the Alpine slopes. Although precipitation during IOP 2b exhibited great horizontal variability, at this time it was nonetheless sufficiently widespread to allow reconstruction of airflow within the Toce and surrounding valleys. Maximum reflectivity values of ~45 dBZ were observed within the most intense cells, with no evidence of widespread stratiform precipitation during the period of aircraft investigation. Several elongated convective bands oriented approximately parallel to the low- to midtropospheric flow are evident over the elevated terrain adjacent to the Toce River valley, consistent with the finding by Medina and Houze (2003) that convective precipitation during IOP 2b was initially triggered over the rapidly rising lower slopes of the Alps. In agreement with single-Doppler observations described by Steiner et al. (2003), an unequivocal description of the *up*-valley nature of flow at this time is obtained (Fig. 4a). Moreover, the fully three-dimensional vector flow field afforded by the Electra's airborne dual-Doppler coverage extending above and beyond the narrow valley walls shows a mostly uniform flow at low- and midlevels that rose freely up and over the steep terrain, possessing relatively weak vertical shear in the barrier-normal direction (Fig. 4b). In tandem with larger-scale analyses discussed by Medina and Houze (2003; see especially their Figs. 3a and 5b), this result confirms that low-level moist southerly flow originating over the Mediterranean Sea during IOP 2b reached the Alpine barrier virtually unimpeded, where it supported development of sustained, locally intense convective precipitation, resulting in some of the heaviest daily rainfall accumulations observed during the MAP experimental period [>300 mm $(24\ h)^{-1}$]. Of interest is that Fig. 4 also reveals a reflectivity *minimum* within the Toce, although hydrological processes may still account for great impacts in such valleys because floodwaters ultimately course through them. Thus, no persistent convective response to airflow being channeled up valley [e.g., of the kind described by Caracena et al. (1979) in the case of the Big Thompson Canyon storm] was noted in the upper reaches of the Toce River valley.

Because of the strongly cellular character of precipitation and isolated nature of echoes over the Lago Maggiore region at this time, complete reconstruction of airflow throughout the Lago Maggiore region was not possible in a ''snapshot'' sense. Nonetheless, glimpses of the horizontal airflow pattern retrieved within other valleys (not shown) strongly suggest that the up-valley nature of the flow was not specific to the Toce.

c. A case of stratiform precipitation (MAP IOP 8)

Because different precipitation regimes and radar platforms may present different challenges to the analysis of airborne Doppler data, it is instructive to consider a second, contrasting example. A particularly illustrative case is presented by an extensive dataset collected by the NOAA P-3 on 21 October 1999 during MAP IOP 8,

Unauthenticated | Downloaded 03/11/24 09:28 PM UTC

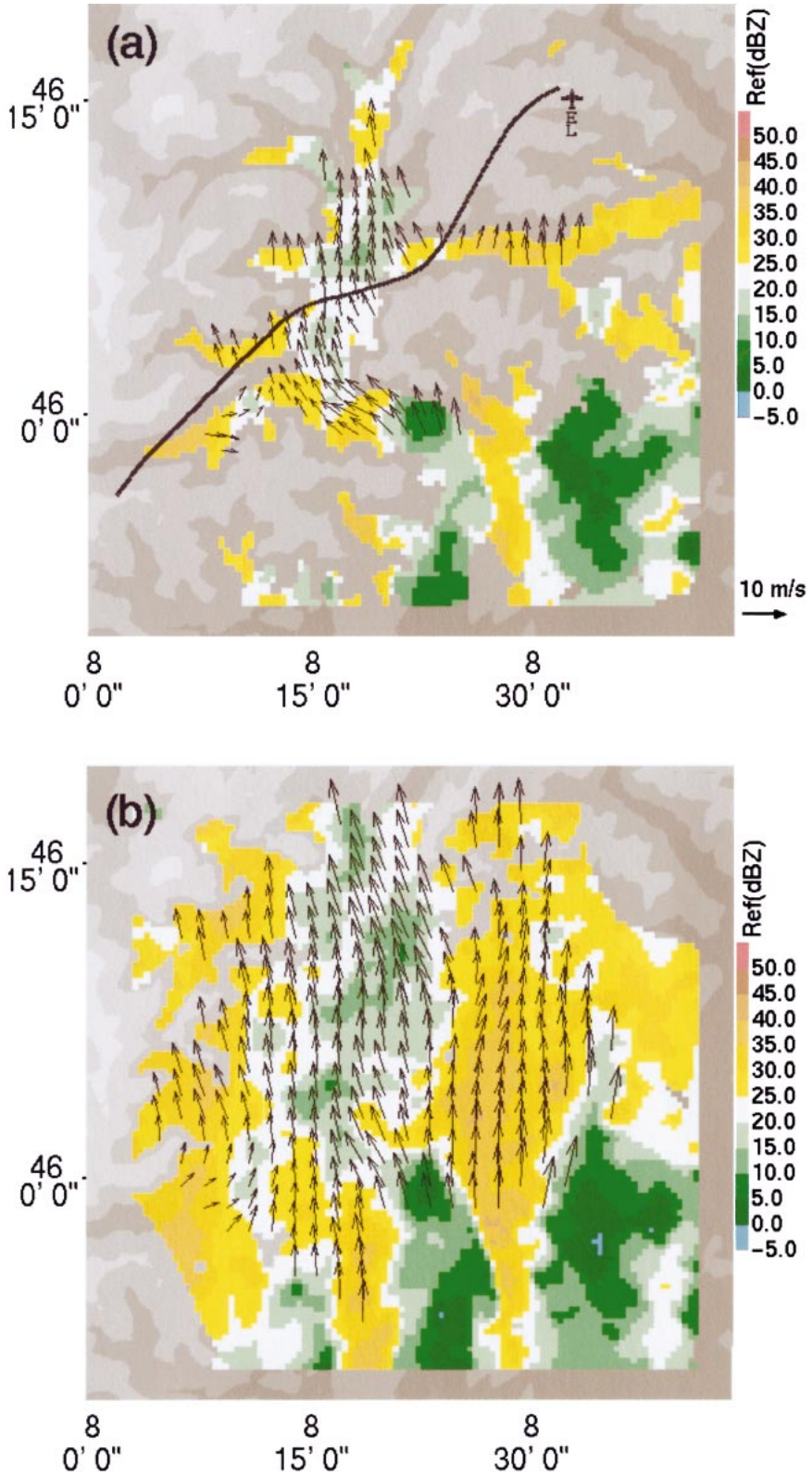

FIG. 4. Airborne dual-Doppler analysis of absolute flow [vectors, key at lower-right of (a)] and reflectivity (color shading, dBZ) over a displayed domain of approx 40 km × 40 km encompassing the Toce River valley, as derived from ELDORA observations at 0933–0938 UTC 20 Sep 1999 at (a) 1 and (b) 2 km MSL. Horizontal and vertical resolutions are 0.5 and 0.25 km, respectively.

Unauthenticated | Downloaded 03/11/24 09:28 PM UTC

when yet another strong baroclinic system passing eastward across the Alps produced significant orographic precipitation. In this case, however, the presence of a preexisting cool and extremely stable low-level air mass assisted formation of persistent widespread precipitation not only over the climatologically favored slopes of the Lago Maggiore region, but also over an adjacent zone of flat terrain extending almost 200 km upstream of the Alpine barrier (Bousquet and Smull 2003). Over the landmass of northern Italy and southern Switzerland, precipitation was essentially stratiform because of the presence of a deep layer of cool, blocked flow at low levels that prevented more unstable low-level air originating over the Mediterranean Sea from reaching the Alpine barrier (Bousquet and Smull 2003; Medina and Houze 2003; Rotunno and Ferretti 2003). As part of the horizontally extensive dataset collected on this day, the P-3 executed several northeast-bound tracks over the Toce River valley (Fig. 5) that were analogous to the single track flown there by the Electra during IOP 2b (cf. Fig. 4).

Figure 5 presents the horizontal wind and reflectivity fields derived from the analysis of two datasets collected on 21 October 1999 both within and surrounding the Toce River valley at 0911–0916 (left-hand panel) and 0950–0955 UTC (right-hand panel), respectively. At the time of the P-3-based investigation, the Toce was entirely filled with precipitation, which exhibited some tendency to be organized in elongated southwest–northeast bands. As may be expected from the appearance of raw data collected during the first time interval (Fig. 1), analyzed reflectivity values over and immediately adjacent to the terrain were homogeneous and stratiform in nature. Although other views of reflectivity show systematic variations on a broader scale over and adjacent to the Alpine slopes (Bousquet and Smull 2003), no systematic variations in inferred rain rates are seen within the confines of the Toce River valley at this time. The relative absence of evolution in the precipitation field during the 45-min interval that separates the two analyses is a strong indication of the long-lasting character of the precipitation adjacent to the Alps on this day, as already noted by Medina and Houze (2003) and Bousquet and Smull (2003).

If description of the reflectivity structure deep within this narrow valley attests to the ability of airborne radars to investigate small-scale precipitation features over mountainous regions, an even more powerful illustration of this capability lies in the ability to recover 3D airflow over extremely rugged terrain. Our analysis provides a detailed description of airflow throughout virtually the entire extent of the Toce and other deep, tortuous valleys carved into the southern face of the Alps. Analyzed low-level winds (Figs. 5a,b) reveal a pronounced down-valley component sweeping through the entire sampled extent of the Toce drainage. The 3D airborne Doppler results trace this down-valley current into multiple narrow tributaries of the Toce and also illustrate its connection to the unconstrained more spatially complex southeasterly flow pattern aloft (Figs. 5c,d), where a pronounced zone of flow deformation and associated convergence is observed in the transition between down-valley flow and overriding southeasterly winds from the Po River valley. This flow then progressively veered to southerly with height (Figs. 5e,f). Aided by contributions from multiple side valleys, down-valley flow speeds initially near $\sim$3–5 m s^{-1} at the valley's upper end (where the analysis extends to within 15 km of the Alpine crest) accelerated to $\sim$10 m s^{-1} near the mouth of the Toce, where it met more quiescent easterly-component flow along the northern limit of the Po River basin.

Vertical cross sections of radar reflectivity and absolute airflow through the lower part of the Toce (in a direction approximately parallel to the northwest–southeast-oriented lower portion of the valley) are presented in Fig. 6 for both analysis times. The vertical reflectivity structure (Figs. 6a,b) shows precipitation extending up to 7 km altitude (the top of the analysis domain), and a well-defined bright band, indicative of melting precipitation, intercepting the terrain over the massif. The implied downward slope of the 0°C isotherm, ranging from 2.25 km MSL above the Toce's mouth to 1.75 km MSL over the Monte Rosa massif, suggests that the coolest air was concentrated along the base of the Alps. An elevated reflectivity maximum, likely to be associated with precipitation advected from the central Po River valley, was observed at approximately 4 km MSL at 0910 UTC (Fig. 6a), but, overall, precipitation was strongly stratiform with no apparent sign of convective activity over either the mountains or adjacent flat terrain.

The component of the wind in the plane of the section (Figs. 6c,d) was also strongly stratified. Within the lower part of the Toce, the down-valley flow (negative values in Figs. 6c,d) was observed up to about 1.5 km MSL but extended up to 2 km MSL at the northwest (i.e., right) edge of the section. Hence, downslope flow was not necessarily confined just to the deep valleys but also occurred over some intervening slopes, as will be further illustrated later. Immediately above this layer of northerlies, strong unconstrained southeasterly winds were observed up to the top of the analysis domain. The vertical tilt of the east-southeasterly flow maximum along the plane of this section suggests that, despite its stable nature, low-level airflow was apparently able to rise over the terrain. As shown by Bousquet and Smull (2003), however, the lifting was initiated some distance away from the barrier as underlying strong easterly winds originating from the eastern Po River valley led

←

For legibility, vectors are plotted at only every third grid point. Underlying gray shading represents digitized terrain height commencing at 0 m MSL (dark shading) in steps of 750 m. Black line in (a) indicates NCAR Electra flight track.

Unauthenticated | Downloaded 03/11/24 09:28 PM UTC

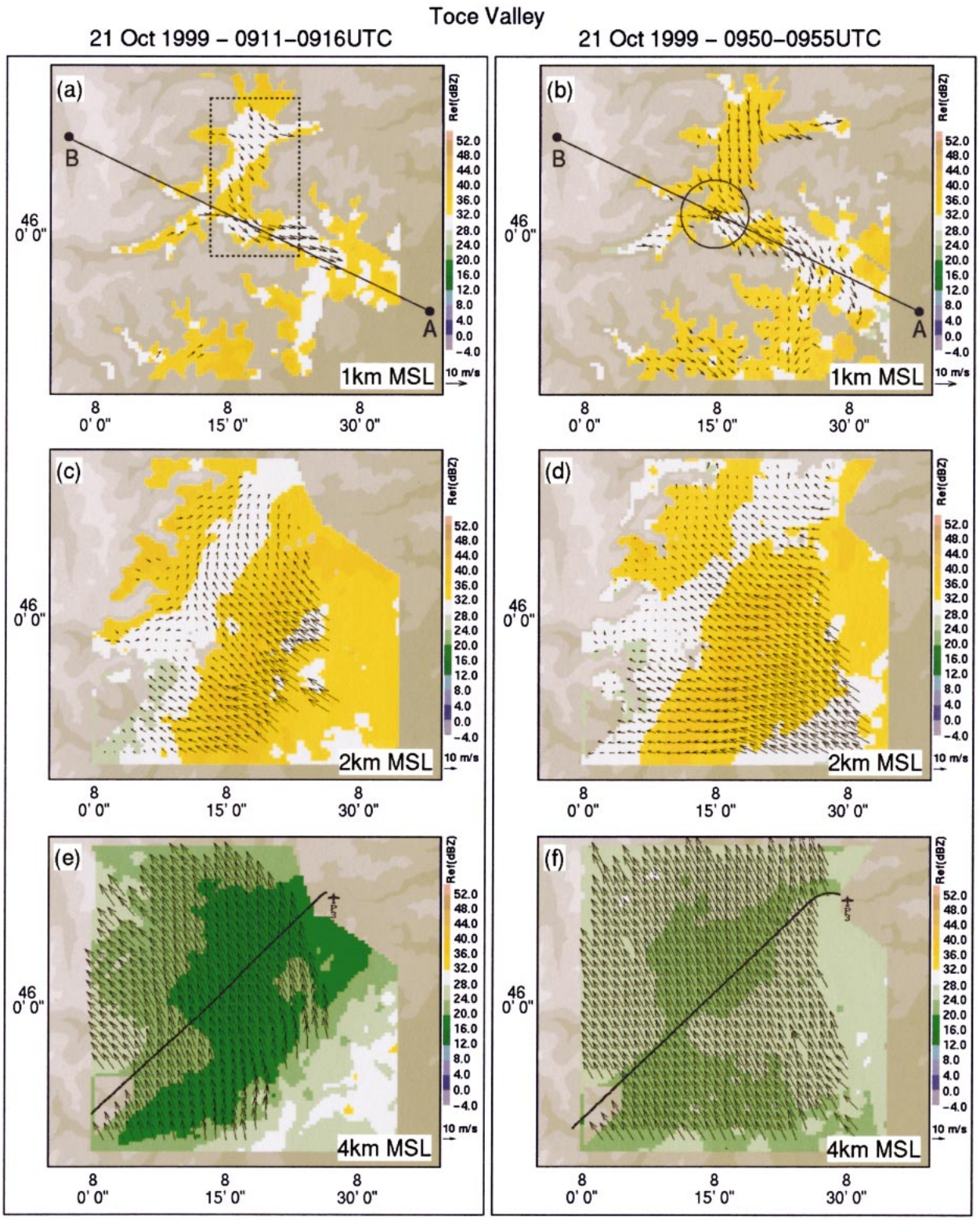

FIG. 5. As in Fig. 4, but for northeast-bound P-3 tracks during intervals (left) 0911–0916 and (right) 0950–0955 UTC on 21 Oct 1999. Airflow (vectors, key at lower right) and reflectivity (color shading, dBZ) at (a), (b) 1.0, (c), (d) 2.0, and (e), (f) 4.0 km MSL, respectively; are shown. Note the different scaling vectors in (a), (b) and (c)–(f). Black line segment AB in (a), (b) denotes horizontal projection of the vertical section presented in Fig. 6. Black dashed rectangle in (a) indicates the domain where mean vertical profiles presented in Fig. 8 are computed. Black circle in (b) indicates the domain within which DOW and P-3 data presented in Fig. 7 were averaged. Black lines in (e), (f) indicate NOAA P-3 flight track.

Unauthenticated | Downloaded 03/11/24 09:28 PM UTC

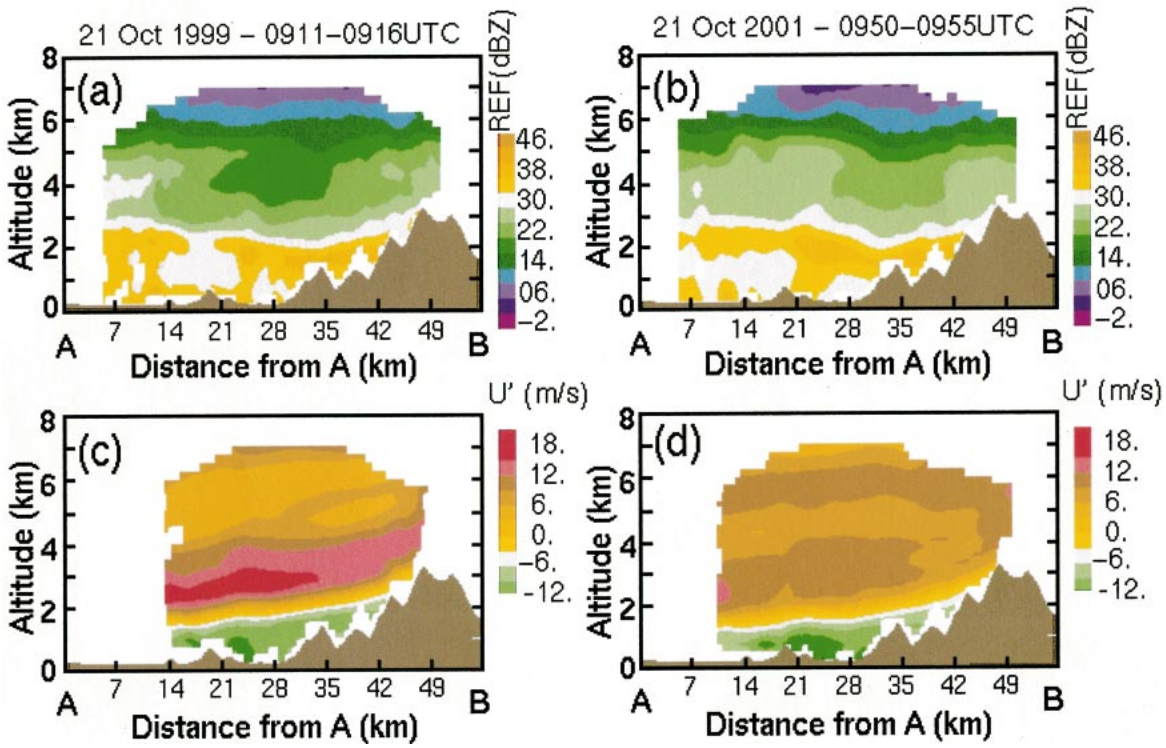

FIG. 6. Vertical cross section of (top) radar reflectivity and (bottom) airflow in the plane of the section AB indicated in Fig. 4, based upon data collected over intervals (left) 0911–0916 and (right) 0950–0955 UTC 21 Oct 1999. Dark shading indicates underlying topography.

to a deep layer of blocked flow accumulating within the Po basin. Consistent with Fig. 5, wind and precipitation structures within the valley and immediately above the slopes did not undergo strong evolution during the time interval (45 min) that separates the two analyses, even as the strength of the unconstrained rising midlevel southeasterly flow evidently decreased from 21 to 15 m s^{-1} in association with the approach of the upper-level trough axis. Likewise, observed low-level reflectivity structures were similar.

During IOP 8, the DOW radar (Wurman et al. 1997) was also centrally deployed near the sharp bend in the L-shaped Toce at Pieve Vergonte (cf. Fig. 3), providing temporally continuous observations of the flow within this valley (Steiner et al. 2003) and an independent source of high-resolution observations that can be used to validate P-3 radar-derived observations over this region. Figure 7 (adapted from Steiner et al. 2003) presents vertical profiles of reflectivity (Fig. 7a), wind speed (Fig. 7b), wind direction (Fig. 7c), and divergence (Fig. 7d) up to an altitude of 4.5 km MSL as derived from both P-3 and DOW observations at 0950–0955 UTC. DOW profiles were obtained from velocity–azimuth display analyses (Browning and Wexler 1968; Matejka and Srivastava 1991) at ~0950 UTC, within a radius of 5 km from the radar (Fig. 3). For comparison purposes, 3D wind and reflectivity fields inferred from P-3 observations were averaged within a similarly sized 10 km × 10 km domain centered on the DOW location. Overall, the agreement between the two radars is excellent, attesting to the extreme quality of 3D wind and reflectivity fields that can be obtained from airborne systems over complex terrain. Both analyses clearly show the existence of a bright band between 1.75 and 2 km MSL (Fig. 7a) in association with a layer of convergence (Fig. 7d) approximately collocated with the melting layer. Vertical profiles of wind speed and direction (Figs. 7b,c) are consistent in showing northerly winds (viz., down-valley flow) up to an altitude of 1.75 km MSL. As also seen in Figs. 7a, and 7b, the uppermost limit of the downslope flow was very near the bright-band level, where melting contributed to the stabilization and diabatic cooling of air that was identified by Steiner et al. (2003) as the dominant driving mechanism for down-valley flow.

To complement these results, Fig. 8 shows vertical profiles of mean divergence (Fig. 8a) and derived vertical velocity (Fig. 8b) derived from airborne observation at both analysis times within a domain of 15 km × 30 km that encompasses the entire sampled extent of the Toce River drainage (Fig. 5a). In its basic modality, the structure of mean divergence profiles within the valley is similar to that obtained within the smaller domain centered on Pieve Vergonte, with overall mean divergence below and aloft a 1.5-km-deep convergence layer at ~1.5 km MSL. Consistent with the orographic (vs convective) nature of the forcing involved, however, the overall depth subtended by these signatures (~4–6 km)

Unauthenticated | Downloaded 03/11/24 09:28 PM UTC

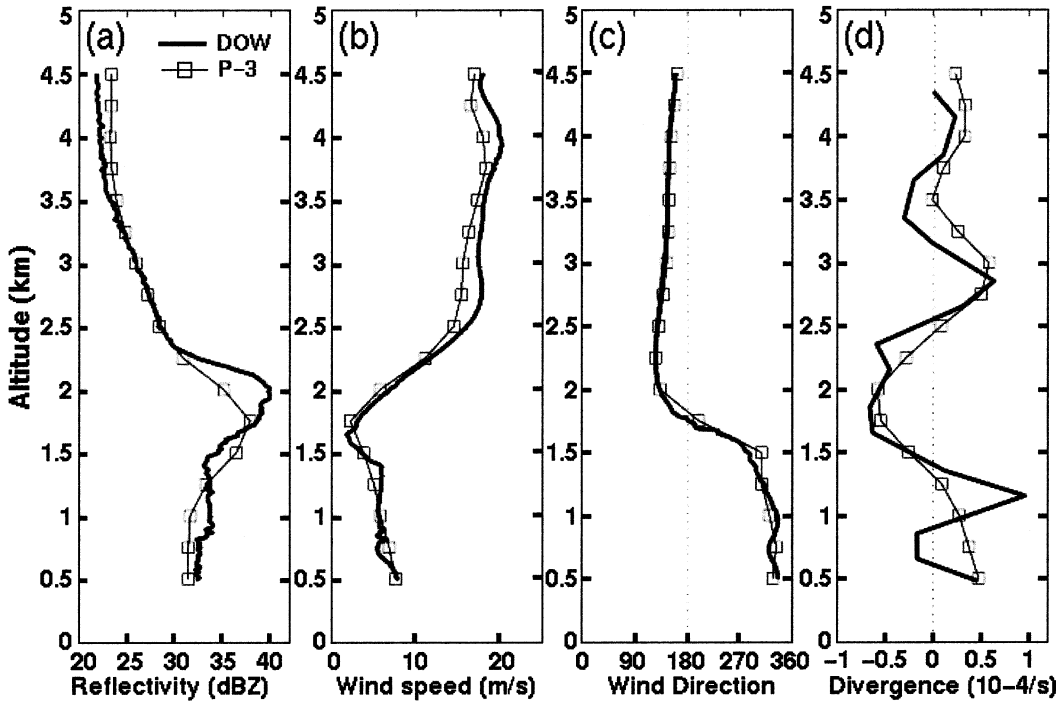

FIG. 7. Vertical profiles of mean (a) radar reflectivity, (b) wind speed, (c) wind direction, and (d) divergence as derived from DOW (heavy black line) and NOAA P-3 (squares) observations at approx 0950 UTC 21 Oct 1999, within the circular domain indicated in Fig. 5b. Adapted from Steiner et al. (2003).

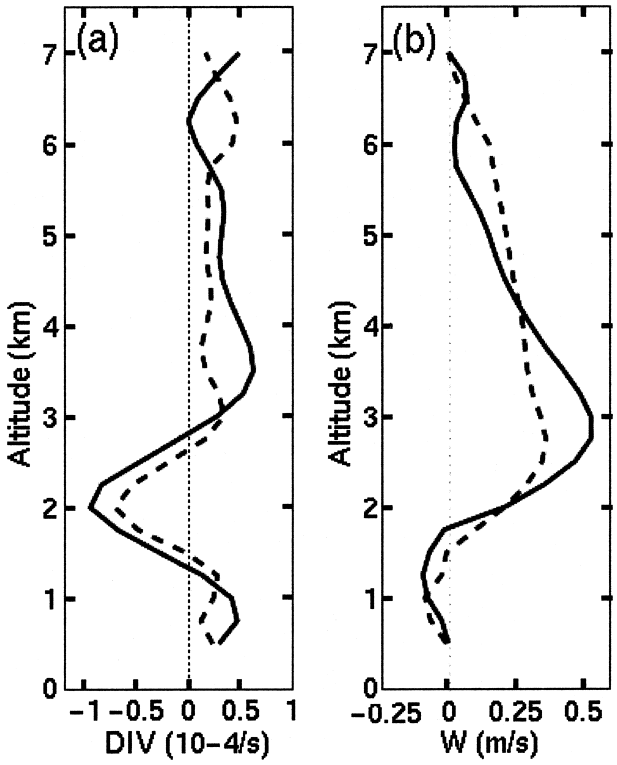

FIG. 8. Vertical profiles of (a) mean divergence and (b) mean vertical velocity within the Toce valley (the averaging domain is outlined in Fig. 5a) as derived from NOAA P-3 analyses at 0911 (solid) and 0950 UTC (dashed) 21 Oct 1999.

is relatively limited in comparison with that seen in mesoscale convective systems (frequently ~10 km). Estimated midlevel convergence was slightly stronger at 0910 UTC, consistent with the relatively stronger midlevel winds observed impinging upon the terrain at this time (Figs. 5c,d). At both times, the mean vertical velocity profile exhibits a clear downdraft/updraft structure similar to that commonly observed within the stratiform region of mesoscale convective systems (e.g., Leary and Houze 1979; Mapes and Houze 1995; Bousquet and Chong 2000). Within the valley, weak downward motions were diagnosed, presumably in response to negative buoyancy generated by both melting and evaporation of precipitation particles below the 0°C isotherm (Fig. 7a) and dynamic blocking, which forced the stable air impinging on the barrier to subside and concentrate within the drainage. Aloft, upward motions in the order of a few tens of centimeters per second were observed as air, initially lifted over the Po River valley, gently rose over the Alpine terrain (Bousquet and Smull 2003).

Using the DOW radar, which provided an uninterrupted view of conditions within the Toce during the full duration of MAP IOP 8, as well as other sources of observations, Steiner et al. (2003) drew a clear and unique picture of the down-valley flow life cycle within this valley. However, because of difficulties in operating a truck-mounted instrument in a complex environment such as the Alpine region, DOW could not be moved

Unauthenticated | Downloaded 03/11/24 09:28 PM UTC

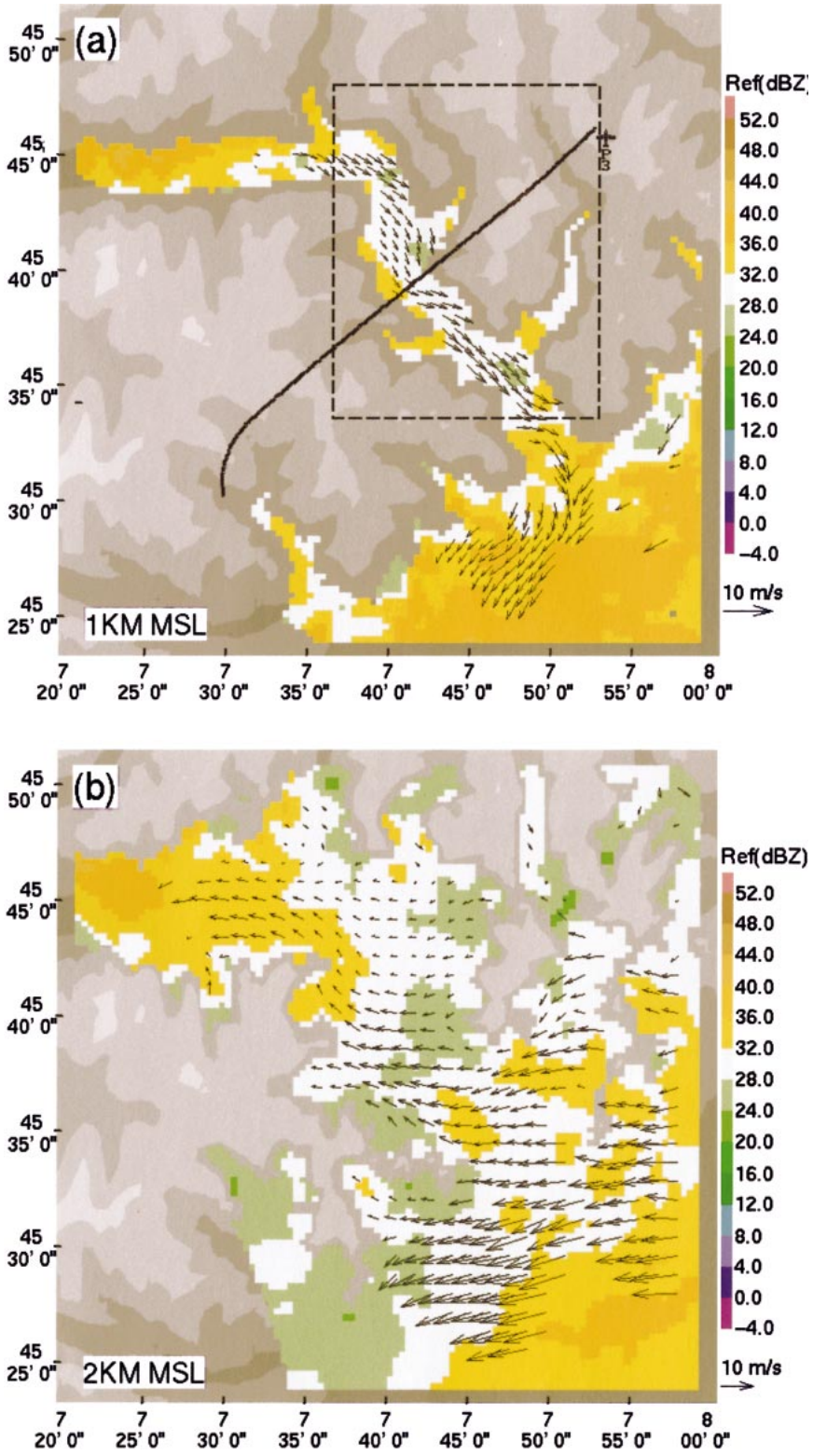

FIG. 9. As in Fig. 4, but for a domain of approx 45 km × 45 km centered on the Val d'Aosta, as derived from a northeast bound P-3 track during the interval 0906–0910 UTC at (a) 1 and (b) 2 km MSL. Note the different scaling vectors in (a) and (b). Black line in (a) indicates the NOAA P-3 flight track. In (a), the dashed box indicates the domain for which mean vertical profiles presented in Fig. 10 are computed.

Unauthenticated | Downloaded 03/11/24 09:28 PM UTC

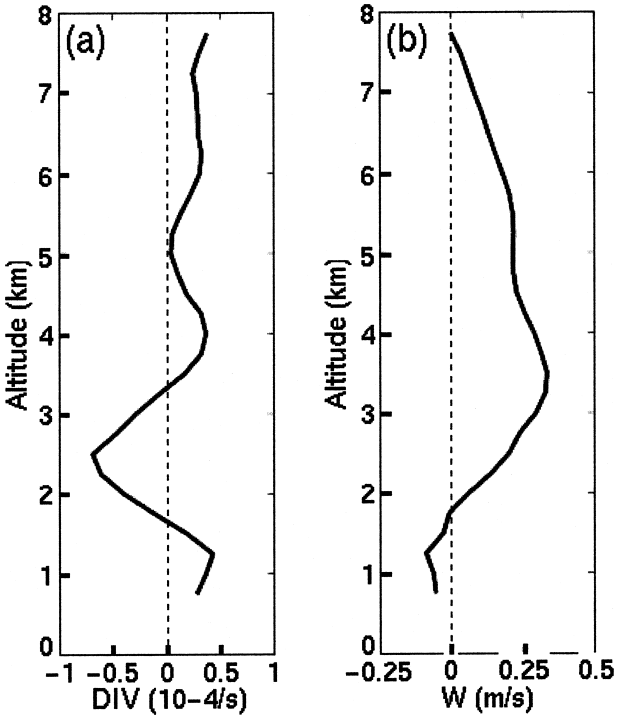

FIG. 10. As in Fig. 7, but for the time interval 0906–0910 UTC, over the domain shown in Fig. 9.

during the course of an IOP, and valley flow observations during MAP IOP 8 were thus restricted to the Toce. Thanks to their almost unlimited mobility, airborne radar systems provide a unique opportunity to investigate the behavior of airflow within other drainages of the Lago Maggiore region and, hence, to extend the findings of Steiner et al. (2003) for IOP 8 to other Alpine valleys.

Another major Alpine rift that can be identified in Fig. 3 is the Val d'Aosta, which is a narrow and somewhat less acutely bent L-shaped Alpine valley located immediately south of the Monte Rosa massif, about 70 km southwest of the Lago Maggiore. Results of a 3D analysis of observations collected within this valley at 0906–0911 UTC are presented in Fig. 9. Here again, the low-level airflow was directed in a downslope sense, away from the mountains and into the Po basin (Fig. 9a). As opposed to the Toce (Fig. 5), within which a strong flow acceleration could be noticed between the upper and lower ends of the valley, the airflow within the Val d'Aosta was relatively uniform (possibly because of the absence of large tributaries), with values ranging from 4 m s^{-1} in the upper part of the valley to 6 m s^{-1} near the mouth of the valley. At this point the downslope flow was found to merge with a cool, blocked northeasterly flow paralleling the Alps. At midlevels (Fig. 9b), airflow was relatively uniform over the plain but still strongly channeled over the mountains in response to the influence of the Monte Rosa massif.

Because the two valleys present similar characteristics, it is instructive to compare further the vertical structure of airflow within the Val d'Aosta with respect to that within the Toce River valley. Figure 10 presents vertical profiles of mean divergence and vertical velocity within a domain that encompasses the lower (northwest–southeast oriented) part of the Val d'Aosta (Fig. 9a). Of particular interest is that the vertical structure of the wind shows strong similarities from one valley to the other, such as the existence of a layer of strong convergence at midlevels (Fig. 10a), as well as mean subsiding motions within the valley (Fig. 10b). Note, though, that the midlevel convergence layer was deeper over the Val d'Aosta region. This difference probably resulted from the existence of the Monte Rosa massif to the north, whose presence forced the stable midlevel flow impinging on the barrier to decelerate (Fig. 9b) and led to additional convergence above 2.5 km MSL. However, these results support that mechanisms identified by Steiner et al. (2003) to be responsible for the formation of down-valley flow near Pieve Vergonte apply not only to the entire extent of the Toce (Fig. 8) but also to other valleys.

Further evidence for the highly pervasive nature of down-valley flow within multiple valleys of the Lago Maggiore region is provided in Fig. 11, which encompasses the region extending east of the Toce over the Lago di Como (cf. Fig. 3). The strong tendency for flow to be constrained by the local valley orientation (and in no sense constrained by the analysis method itself) is immediately apparent. Moreover, a companion east–west vertical cross section of the meridional flow component (Fig. 12) that encompasses multiple valleys and intervening slopes illustrates both the overriding southerly winds and their ultimate reversal in response to higher terrain to the north as some portion of this incident flow was blocked, subsided, and was diverted southward. Within the sampled layer, which extended to within several hundred meters of the surface, the intensity of return flow was inversely proportional to height. As such, down-valley flow was focused (though sometimes asymmetrically) along the axis of individual valleys but notably also enveloped intervening slopes up to an elevation near 2 km MSL.

4. Conclusions

Owing to recent advances in signal processing and their characteristic mobility and flexibility, airborne Doppler radars are increasingly being relied upon for investigation of weather systems in highly remote and challenging environments, such as intense storms that occur over rugged mountainous terrain. This ability implies unique challenges in terms of data analysis, however, including the advent of huge datasets resulting from fast sampling rates along extensive flight tracks, as well as complex data-processing issues that hinge upon the large number of degrees of freedom for an airborne platform employing vertical scanning strategy. In addition, observations collected in these environ-

Unauthenticated | Downloaded 03/11/24 09:28 PM UTC

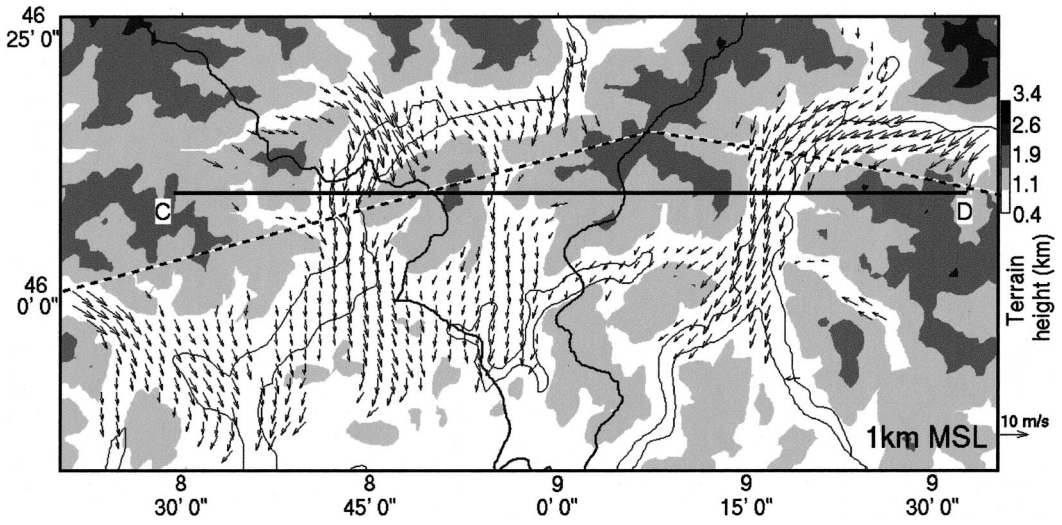

FIG. 11. Airborne dual-Doppler analysis of absolute airflow (vectors, key at lower right) at a height of 1 km MSL within an approx 100 km × 40 km area based upon data collected during the interval 1255–1310 UTC 21 Oct 1999. Gray shading indicates terrain elevation (km MSL) according to key at right. Dashed line indicates P-3 flight track. Black line segment (CD) denotes horizontal projection of the vertical section presented in Fig. 12.

ments present an especially formidable challenge to traditional manual interactive editing methods because of the highly irregular and, at times, ambiguous nature of surface and second-trip echo returns.

This paper has presented a new, largely automated approach to preprocess airborne Doppler radar measurements collected over mountainous terrain by identifying and eliminating sources of data contamination both at the earth's surface and in the free atmosphere through a combination of data renavigation, pattern recognition, reliance upon high-resolution digital terrain information, and application of a more familiar running-mean algorithm. Detailed examination of data in their native polar coordinates (i.e., ''radar space'') has revealed the excellent reliability of this method in removing most sources of error.

To investigate the potential of airborne observations to provide detailed descriptions of airflow over steep terrain and to evaluate further the performance of this editing technique in a Cartesian framework, extensive applications have been carried out for data collected by the NOAA P-3 and NCAR ELDORA during the Mesoscale Alpine Programme experiment (Bougeault et al. 2001) by ingesting numerous edited datasets in the

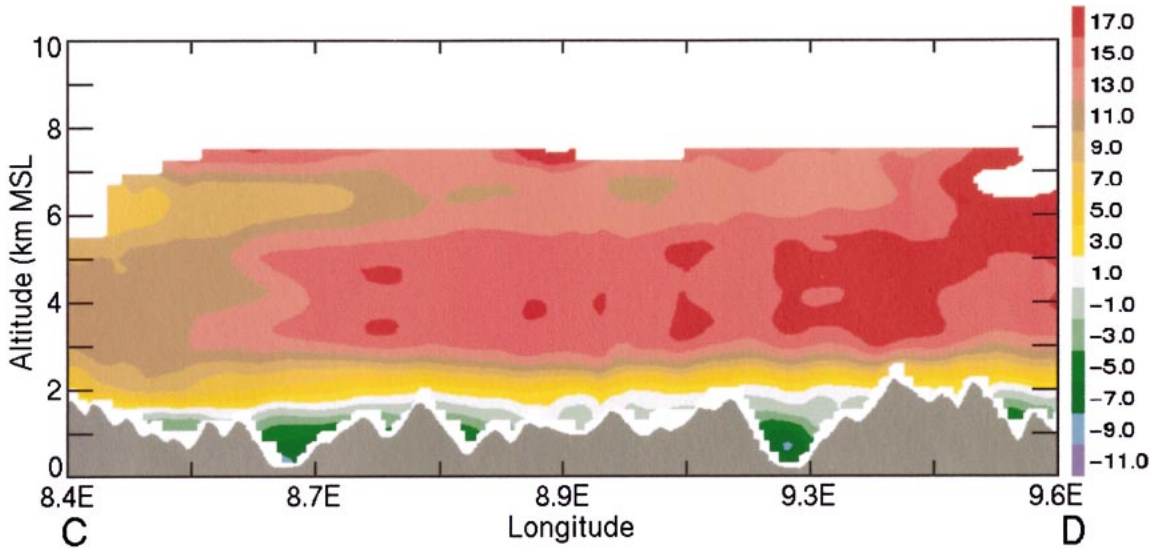

FIG. 12. Zonal cross section of *V* component wind speed along latitude 46.10°N (cf. horizontal projection of section in Fig. 11) at 1255–1310 UTC 21 Oct 1999. Dark shading indicates underlying topography.

Unauthenticated | Downloaded 03/11/24 09:28 PM UTC

MUSCAT analysis (Bousquet and Chong 1998). Analyses produced by this well-suited wind synthesis method have shown a remarkable ability to recover airflow and precipitation fields over and immediately adjacent to the steep Alpine terrain, including deep within several tortuous river valley and their tributaries for two contrasting situations that embody widespread stratiform and intense cellular convective precipitation. Although the application to X-band radar demonstrated herein requires that complex terrain be fully enveloped by precipitation in order for the 3D flow field to be reconstructed, in principle this same technique could be extended to process airborne scanning Doppler lidar data in optically clear environments (e.g., as described by Reitebuch et al. 2001). Such analyses could prove instrumental in efforts to map the transport of pollutants or other aerosols.

These results both confirm and extend single-Doppler measurements from a ground-based platform, as summarized by Steiner et al. (2003). Examples of both freely ascending ''unblocked'' up-valley (as observed on 20 September 1999 during MAP IOP 2b) and down-valley (on 21 October 1999, MAP IOP 8) flow have been illustrated. In the case of MAP IOP 8, the horizontally expansive vector flow fields available only from airborne Doppler perspective have demonstrated unequivocally the pervasive nature of subsiding down-valley winds in a case of profound low-level blocking of airflow upstream of the Alps, which was observed to fill multiple and diversely oriented deep Alpine valleys (and their tributaries) surrounding the Lago Maggiore region. Such flow variations have important implications for orographic precipitation processes and their interplay with features of the larger-scale environmental flow and stratification. The utility of such data to illuminate mesoscale precipitation processes in other complex mountain environments is presently being exploited using data collected by the NOAA P-3 aircraft over the Oregon Cascades during IMPROVE-II and stands to provide a valuable complement to ground-based remote sensors and in situ measurements in evaluating the performance of mesoscale model simulations in a more horizontally expansive way than would otherwise be possible.

Acknowledgments. Data management and software development assistance provided by Stacy Brodzik (University of Washington) and John Daugherty (NOAA/NSSL) are greatly appreciated. Our appreciation is extended to the flight crews of the NOAA P-3 and NCAR Electra, as well as UCAR/JOSS and air-traffic control personnel at the Milano MAP Project Operations Center who made these flights possible. Support provided via award ATM-987502 from the National Science Foundation's Mesoscale Dynamic Meteorology Program, directed by Dr. Stephan Nelson, is gratefully acknowledged. Additional support was provided by the Joint Institute for the Study of the Atmosphere and Ocean (JISAO) under NOAA Cooperative Agreement NA17RJ1232.

REFERENCES

Bargen, D. W., and R. C. Brown, 1980: Interactive radar velocity unfolding. Preprints, *19th Conf. on Radar Meteorology,* Miami, FL, Amer. Meteor. Soc., 278–283.

Bond, N. A., and Coauthors, 1997: The Coastal Observations and Simulations with Topography (COAST) experiment. *Bull. Amer. Meteor. Soc.,* **78,** 1941–1955.

Bougeault, P., and Coauthors, 2001: The MAP special observing period. *Bull. Amer. Meteor. Soc.,* **82,** 433–462.

Bousquet, O., and M. Chong, 1998: A multiple Doppler and continuity adjustment technique (MUSCAT) to recover wind components from Doppler radar measurements. *J. Atmos. Oceanic Technol.,* **15,** 343–359.

——, and ——, 2000: The oceanic mesoscale convective system and associated mesovortex observed on 12 December 1992 during TOGA COARE. *Quart. J. Roy. Meteor. Soc.,* **126,** 189–212.

——, and B. F. Smull, 2003: Observations and impacts of upstream blocking during a widespread orographic precipitation event. *Quart. J. Roy. Meteor. Soc.,* **129,** 391–410.

Browning, K. A., and R. Wexler, 1968: The determination of kinematic properties of a wind field using Doppler radar. *J. Appl. Meteor.,* **7,** 105–113.

Caracena, F., R. A. Maddox, L. R. Hoxit, and C. F. Chappell, 1979: Mesoanalysis of the Big Thompson storm. *Mon. Wea. Rev.,* **107,** 1–17.

Chong, M., and S. Cosma, 2000: A formulation of the continuity equation of MUSCAT for either flat or complex terrain. *J. Atmos. Oceanic Technol.,* **17,** 1556–1565.

——, and O. Bousquet, 2001: On the application of Muscat to a ground-based dual-Doppler radar system. *Meteor. Atmos. Phys.,* **78,** 133–139.

Colle, B. A., and C. F. Mass, 1996: An observational and modeling study of the interaction of low-level southwesterly flow with the Olympic Mountains during COAST IOP 4. *Mon. Wea. Rev.,* **124,** 2152–2175.

——, ——, and B. F. Smull, 1999: An observational and numerical study of a cold front interacting with the Olympic mountain during COAST IOP5. *Mon. Wea. Rev.,* **127,** 1310–1334.

Georgis, J.-F., F. Roux, and P. H. Hildebrand, 2000: Observation of precipitating systems over complex orography with meteorological Doppler radars: A feasibility study. *Meteor. Atmos. Phys.,* **72,** 185–202.

Hildebrand, P. H., C. L. Frush, C. Walther, J. Testud, and F. Baudin, 1994: Design of the ELDORA/ASTRAIA airborne Doppler weather radar: Goals, design, and first field tests. *Proc. IEEE,* **82,** 1873–1890.

Jorgensen, D. P., P. H. Hildebrand, and C. L. Frush, 1983: Feasibility test of an airborne pulse-Doppler meteorological radar. *J. Climate Appl. Meteor.,* **22,** 744–757.

——, T. R. Shepherd, and A. Goldstein, 2000: A multiple pulse repetition frequency scheme for extending the unambiguous Doppler velocity of the NOAA P-3 airborne Doppler radar. *J. Atmos. Oceanic Technol.,* **17,** 535–594.

Leary, C. A., and R. A. Houze Jr., 1979: Melting and evaporation of hydrometeors in precipitation from the anvil clouds of deep tropical convection. *J. Atmos. Sci.,* **36,** 669–679.

Mapes, B. E., and R. A. Houze Jr., 1995: Diabatic divergence profiles in western Pacific mesoscale convective systems. *J. Atmos. Sci.,* **52,** 1807–1828.

Matejka, T. J., and R. C. Srivastava, 1991: An improved version of the extended velocity–azimuth display analysis of single-Doppler radar data. *J. Atmos. Oceanic Technol.,* **8,** 453–466.

Medina, S., and R. A. Houze, 2003: Air motions and precipitation growth in Alpine storms. *Quart. J. Roy. Meteor. Soc.,* **129,** 345–372.

Unauthenticated | Downloaded 03/11/24 09:28 PM UTC

Oye, R., C. Mueller, and S. Smith, 1995: Software for radar translation, visualization, editing, and interpolation. Preprints, *27th Conf. on Radar Meteorology*, Vail, CO, Amer. Meteor. Soc., 359–361.

Pradier, S., M. Chong, and F. Roux, 2002: Radar observations and numerical modeling of a precipitating line during MAP IOP5. *Mon. Wea. Rev.*, **130,** 2533–2553.

Ralph, F. M., and Coauthors, 1999: The California Land-Falling Jets Experiment (CALJET): Objectives and design of a coastal atmosphere–ocean observing system deployed during a strong El Niño. Preprints, *Third Symp. on Integrated Observing Systems*, Dallas, TX, Amer. Meteor. Soc., 78–81.

Reitebuch, O., C. Werner, I. Leike, P. Delville, P. H. Flamant, A. Cress, and D. Engelbart, 2001: Experimental validation of wind profiling performed by the airborne 10-mm heterodyne Doppler lidar WIND. *J. Atmos. Oceanic Technol.*, **18,** 1331–1344.

Rotunno, R., and R. Ferretti, 2003: Comparative analysis of rainfall in MAP cases IOP2b and IOP8. *Quart. J. Roy. Meteor. Soc.*, **129,** 373–390.

Schultz, D. M., and Coauthors, 2002: Understanding Utah winter storms: The Intermountain Precipitation Experiment (IPEX). *Bull. Amer. Meteor. Soc.*, **83,** 189–210.

Steiner, M., O. Bousquet, R. A. Houze, B. F. Smull, and M. Mancini, 2003: Airflow within major alpine river valleys under heavy rainfall. *Quart. J. Roy. Meteor. Soc.*, **129,** 411–432.

Stoelinga, M. T., and Coauthors, 2003: Improvement of Microphysical Parameterizations through Observational Verification Experiments (IMPROVE). *Bull. Amer. Meteor. Soc.*, in press.

Testud, J., P. H. Hildebrand, and W.-C. Lee, 1995: A procedure to correct airborne Doppler radar data for navigation errors using the echo returned from the earth's surface. *J. Atmos. Oceanic Technol.*, **12,** 800–820.

Wurman, J., J. Straka, E. Rasmussen, M. Randall, and A. Zahrai, 1997: Design and deployment of a portable pencil-beam pulsed Doppler 3-cm radar. *J. Atmos. Oceanic Technol.*, **14,** 1502–1512.

Unauthenticated | Downloaded 03/11/24 09:28 PM UTC